Dalton Transactions

Accepted Manuscript

ROYAL SOCIETY OF CHEMISTRY

www.rsc.org/dalton

Cite this: DOI: 10.1039/c0xx00000x

www.rsc.org/xxxxxx

ARTICLE TYPE

Role of oxygen vacancy and Fe–O–Fe bond angle in compositional, magnetic, and dielectric relaxation on Eu-substituted $BiFeO_3$ nanoparticles

Tamilselvan A,[a] Balakumar S,*[a] Sakar M,[a] Chiranjib nayek,[b] Murugavel P,[b] and Saravana kumar K [c]

Received (in XXX, XXX) Xth XXXXXXXXX 20XX, Accepted Xth XXXXXXXXX 20XX
DOI: 10.1039/b000000x

Abstract

Influence of oxygen vacancy on dielectric relaxation behavior of pure and Eu-substituted $BiFeO_3$ nanoparticles synthesized by sol-gel technique has been studied using impedance spectroscopy in the temperature range of 90°C to 180°C. Electric relaxation time and activation energy of oxygen vacancy can be calculated from Arrhenius equation, as found to be 1.26 eV and 1.76 eV for pure and Eu-substituted $BiFeO_3$, respectively. Substitution induces structural disorder and change in Fe–O–Fe bond angle leading to alteration of magnetic properties, observed from magnetic studies and evaluated using Rietveld refinement of XRD patterns. X-ray photoelectron spectroscopy (XPS) confirms the shifting of binding energy of Bi 4f orbital, establishing the Eu substitution at Bi site. Calculation of area under Fe^{2+}/Fe^{3+} (2p) and O (1s) XPS spectra gives approximate values of oxygen vacancy.

Keywords: $BiFeO_3$, Fe–O–Fe bond angle, activation energy, XPS

Introduction

Over the past few years, multifunctional materials have gained much interest of researchers because of their fascinating science and wide range of applications in various fields. Accordingly, multiferroic materials have shown potential applications in many fields such as multiple-state memories, spintronics, transducers, actuators, magneto-electric sensor devices, etc., due to their ferroic properties.[1,2] It is well known that the bismuth iron oxide ($BiFeO_3$) is one of the most well studied and widely discussed multiferroic materials due to its room temperature multiferroic properties with high ferroelectric (830°C) and G type-antiferromagnetic (370°C) transition temperature which makes to study the possibility to explore the suitability of BFO for device applications. $BiFeO_3$ comes under pervoskite structured (ABO_3) family, which crystallizes into distorted rhombohedral structures with space group R3c. Studies have shown that the existence of ferroelectricity in BFO is due to its structural distortion caused by the hybridization of Bi $6S^2$ and oxygen (p) lone pair of electron, and its magnetic properties occur due to Fe ions. If the Fe magnetic moment permits canting of spins, then the antiferromagnetic sub- lattice induces macroscopic magnetization that is called weak ferromagnetism. However, in bulk $BiFeO_3$, existence of space-modulated spin structure that have a wavelength of 62 nm leads to the cancellation of macroscopic magnetization.[3] Besides, BFO suffers from high leakage current that gradually decreases its ferroelectric behavior and dielectric properties. Evidently, many studies have stated that the occurrence of oxygen vacancy defects is common in $BiFeO_3$. Indeed, presence of oxygen vacancy leads to the formation of Fe^{2+} in order to maintain charge balance in the material.[4] Consequently, playing down the oxygen vacancy functionally contributes in the minimization of the leakage current and maximization of net magnetization that can be a beneficial to the multiferroic property of $BiFeO_3$. Aforementioned the problem of oxygen vacancy declines with the modification of Bi or Fe sites through chemical substitution. Some research groups [5-7] have experimented with altering the Bi site through substitution of alkaline earth metals like (Ba, Ca, Sr, etc.) to enhance the magnetic properties of BFO; however, these ions possess 2+ oxidation states and while incorporating them into Bi^{3+} ions resulting in the appearance of oxygen vacancies that in turn increases the electrical conductivity of the material. Hence, several research groups have reported the improved multiferroic property of BFO through chemical substitution of rare earth elements, such as (La, Sm, Ce, Tb, Eu, Dy, and Gd ions)[8-14] owing to their 3+ oxidation state and relatively similar to ionic radius of Bi^{3+}. These in turn would possibly affect the resultant chemically substituted $BiFeO_3$'s structure in its structural distortion. Consequently, it reduces the oxygen vacancy and thereby in enhances the multiferroic property.

It is reported that when rare earth ion Eu^{3+} is substituted in Bi^{3+}ions site, it induces structural distortions owing to its smaller ionic radii (1.07 Å) as compared to Bi ions (1.17 Å).[15] Besides that, Eu ions are of same valence state as that of Bi ions; hence,

there is no possible way to develop oxygen vacancy. Meanwhile, it possibly reduces the secondary phases and oxygen vacancy, thereby improving the ferroelectric and magnetic properties of BFO.

In this work, the effect of Eu substitution on structural, morphological, compositional, magnetic and electric properties of $BiFeO_3$ are studied. Through these characterizations, the author takes the privilege to interpret the results with respect to reduction of oxygen vacancy and enhancements of Fe–O–Fe bond angle with the aim of improve the overall material's multiferroic properties. Hence, we employed simple tartaric-based sol-gel method as synthesized for a single-phase $BiFeO_3$ (BFO) and $Bi_{(1-x)}Eu_xFeO_3$(EBFO) nanoparticles.

Experimental details:

The typical sol-gel[16] technique was employed to synthesize pure and Eu-substituted $BiFeO_3$ compositions. All chemical reagents were of laboratory grade procured from Alfa-Aesar chemical company. Stoichiometric amount of $Bi(NO_3)_3.5H_2O$ and $Fe(NO_3)_3.9H_2O$ were dissolved in double-distilled water with constant addition of conc. HNO_3 in order to get a homogenous solution., Then tartaric acid (as chelating agent) was added to the above solution to obtain the solution of metal and tartaric acid with a molar ratio of 1:2. The obtained solution was vigorously stirred at 80°C for 3 hours to obtain a dry gel resulting in powders. The final products were grind into a fine powder and calcined in a furnace (VB ceramics) at 650°C for 3 hours in order to get pure $BiFeO_3$. The Eu-substituted $BiFeO_3$ compositions were prepared using similar synthesis methodology as that of pure $BiFeO_3$. The difference was the addition of required amount of $Eu(NO_3)_3.H_2O$ in accordance with the substitution percentage. All the synthesized compositions were subjected to thermal gravimetric analysis (Perkin Elmer) in order to identify the approximate annealing temperature range of $BiFeO_3$ phase formation. The samples were heated in an inert atmosphere from room temperature (32°C) to 850°C at the rate of 20°C/min. The structural and phase composition analysis of the samples were carried out in an X-ray diffractometer (XRD, X'PERT PRO PANalytical) using Cu-K_α source (λ = 1.5406 Å) in the 2θ range of 10° to 60° at a scan rate of 3.3°/min.

Field emission electron microscopy (FESEM) was used to study the morphology of the samples (using Hitachi, Japan; Model-S6600). The chemical composition and chemical shift of the elements were determined by using X-ray photoelectron spectroscopy (XPS) instrument (Omicron nanotechnology). Iodometric chemical titration was carried out in order to estimate the oxygen content in the samples. The magnetic properties of the samples were studied at room temperature with an applied field (1 T maximum field) using vibration sample magnetometer (VSM) (using lakeshore). The impedance spectroscopy (IS) measurements were done in an impedance/gain phase analyzer (Solartron, SI 1260) over the frequency range 1 MHz to 1 Hz and temperature range of 40°C to 200°C.

Results and discussion:

Thermal analysis (TGA)

In order to evaluate the calcination temperature, a calculated amount of sample was heated from room temperature to 850°C in an inert atmosphere at a rate of 20°C/min. At 800°C, the estimated weight loss was 38% as depicted in Fig.1. The weight loss observed at 100°C, 200°C and 400°C were due to the removal of water, CO_2 and tartaric acid, respectively.[17] The constant weight loss after 500°C enabled to fix 650°C as calcination temperature. Therefore, all the as prepared samples were calcined at an optimized temperature of 650°C for 3 hours and obtained the BFO phase.

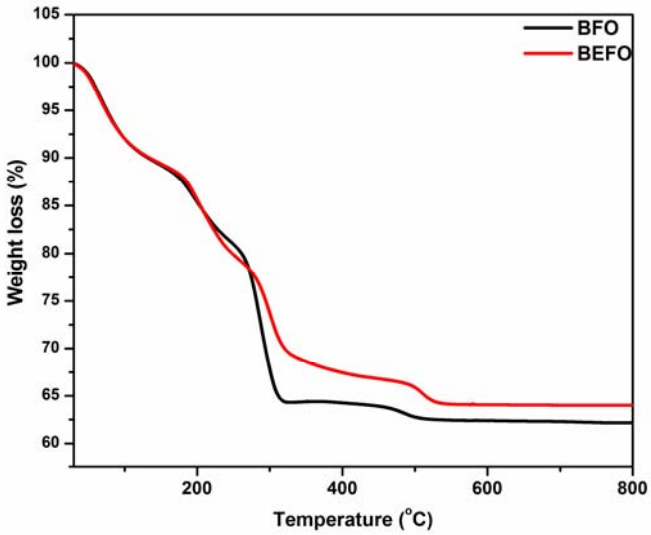

Fig.1 TGA curves of BFO and EBFO

Structural analysis

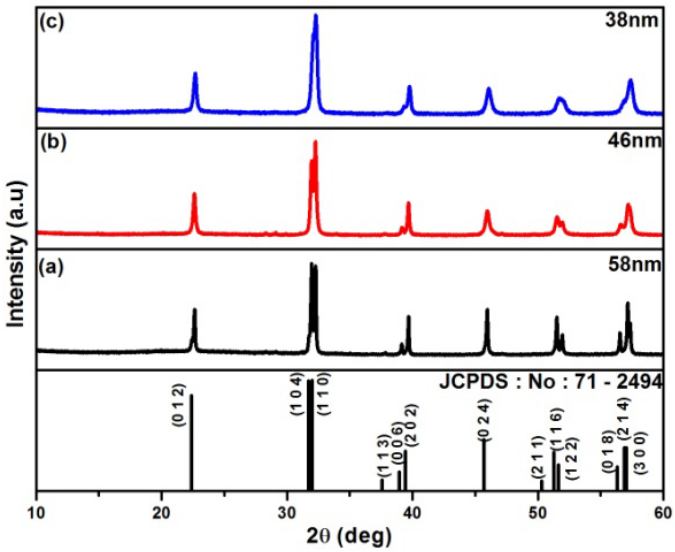

Fig.2 (a) XRD pattern of (a) BFO (b) $Bi_{0.95}Eu_{0.05}FeO_3$ and (c) $Bi_{0.90}Eu_{0.10}FeO_3$

Fig 2(a) shows the XRD pattern of $Bi_{1-x}Eu_xFeO_3$ ($0 \leq x \leq 0.10$) compositions. All the reflections peak were indexed to rhombohedral space group R3c. Notably, the observed merge of planes (104) and (110) in 10% Eu-BFO as shown in Fig. 2 (b) indicated the lattice distortions occurred in the composition. These lattice distortions showed possible influence in lattice parameter of Eu-substituted BFO compositions. Therefore, in

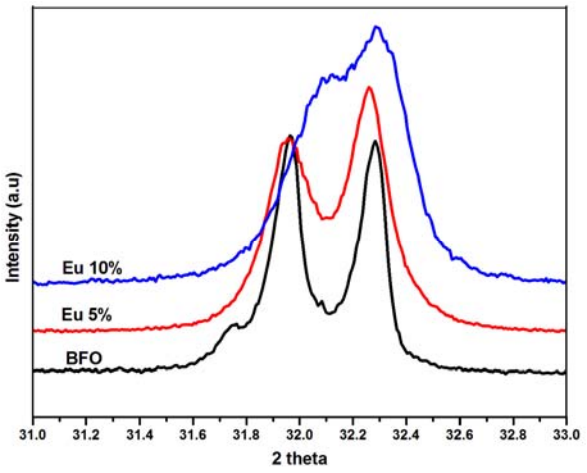

Fig.2 (b) Merges of plane (1 0 4) and (1 1 0)

order to confirm the distortion, the XRD patterns were analyzed using Rietveld refinement method using FULLPROF PROGRAM to calculate the lattice parameters, Fe–O bond length, and Fe–O–Fe bond angle. "For all the refinement, Thompson-Cox-Hastings pseudo-Voigt function was chosen and background was fitted with 6-Coefficient polynomial function. Lattice parameter, scale factor, background, atomic position FWHM/shape parameter, asymmetric parameter etc were refined and micro strain parameter refinement was not done during refining process". Figure 3 shows the observed, calculated, and the difference in the refined XRD patterns of BFO and EBFO. The obtained values of the lattice parameters for pure BFO are a = b = 5.5793 Å and c = 13.8685 Å, which are consistent with the reported values.[18] Detailed analysis of the structural parameters studied using Rietveld refinement are given in Table 1

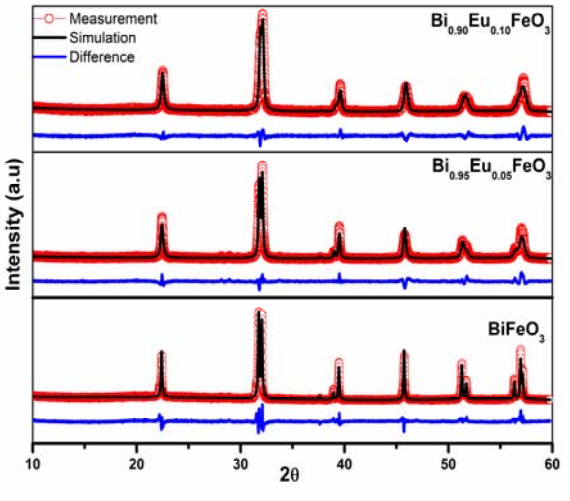

Fig.3 Rietveld Refinement of BFO and EBFO samples

The 10% Eu-substituted BFO showed no effect on its crystal structure but lattice parameters decreased with Eu percentage, in accordance with the literature reports. [19] Therefore, a decrease in unit cell volume (Table 1) was observed, probably due to the smaller ionic radii of Eu^{3+} compared to Bi^{3+} ions leading to the merging of peaks. Using Scherer`s formula the average crystallite size of BFO, $Bi_{0.95}Eu_{0.5}FeO_3$, and $Bi_{0.9}Eu_{0.1}FeO_3$ are calculated to be 58 nm, 48 nm, and 38 nm, respectively.

Table 1 The refined structural parameters of BFO and EBFO samples based on the measured XRD patterns shown in Fig. 2(a)

Parameter	$BiFeO_3$	$Bi_{0.95}Eu_{0.05}FeO_3$	$Bi_{0.90}Eu_{0.10}FeO_3$
a	5.5793	5.5762	5.5661
b	5.5793	5.5762	5.5661
c	13.8685	13.8475	13.783
α	90	90	90
β	90	90	90
γ	120	120	120
Volume	373.8	372.8	369.8
R-Factor			
R_p	5.34	5.70	5.52
R_{wp}	7.08	7.61	6.95
χ^2	6.33	5.33	3.94
Atomic position – Bi	Bi	Bi/Eu	Bi/Eu
x	0	0	0
y	0	0	0
z	0	0	0
Atomic position – Fe			
x	0	0	0
y	0	0	0
z	0.2787	0.2207	0.2210
Atomic position – O			
x	0.4497	0.5600	0.56986
y	0.0069	0.014	0.0297
z	1.0457	0.9613	0.9600
B iso(Bi)	0.273	0.2622	0.2046
Fe	0.396	1.120	0.9956
O	0.8106	1.141	0.672
		(Bi/Eu – O)	(Bi/Eu – O)
Bi–O bond length	2.3674	2.3779	2.298
Fe–O bond length	1.85	1.9852	1.981
Fe–O–Fe bond angle	159.9	161.63	158.78

Morphological Analysis

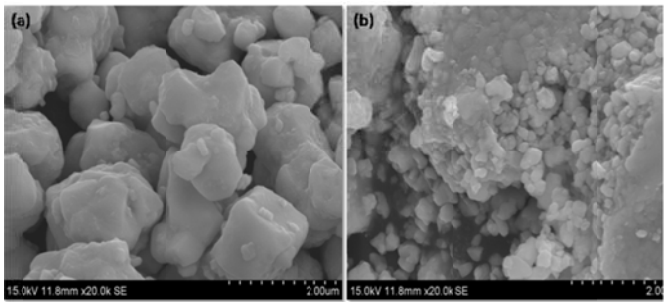

Fig.4 FESEM images of (a) BFO and (b) EBFO samples.

Fig. 4 Shows the FESEM micrographs of BFO and EBFO. The BFO sample possessed irregular morphology and found to be agglomerated particles, while EBFO composition possessed nearly spherical particles relatively less agglomerated particles. Fig.5 illustrates the high resolution TEM image of pure BFO. The observed lattice fringes confirmed that pure BFO was well crystallized and the selected area electron diffraction (SAED) pattern, as shown in inset of fig. 5, was also substantiated this observation.

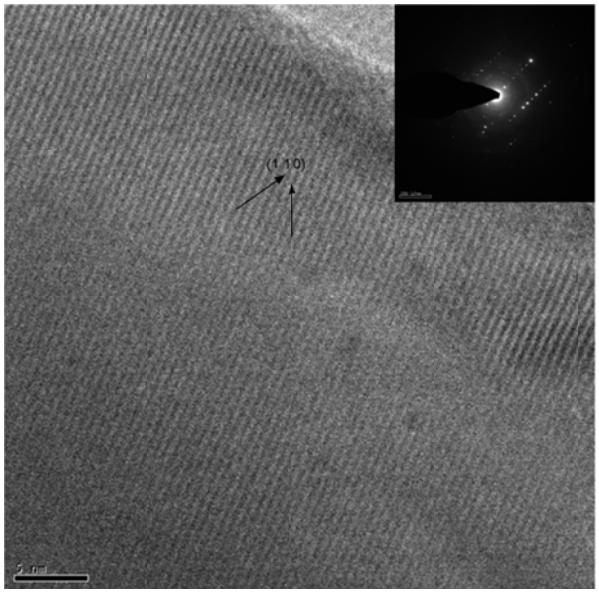

Fig.5 HRTEM images and SAED pattern of BFO.

Chemical analysis by XPS

In order to identify the element, chemical shift, oxidation state of Fe, and oxygen vacancy of the pure and Eu-substituted BFO samples, detailed XPS analysis was carried out. XPS survey spectra of pure and Eu-substituted BFO samples are presented in Fig. 6. This reveals the presence of Bi, Fe, O, and Eu without any other trace impurities except for the small amount of carbon. This confirms the chemical compositions of pure and Eu-substituted BFO samples. For narrow scan spectra, C 1s peak is taken as reference for the calibration of binding energy values obtained for the elements. In 10% Eu-substituted BFO, Eu ions affect the binding energy value of Bi leading to a change in the Bi–O binding energy when compared to pure BFO.

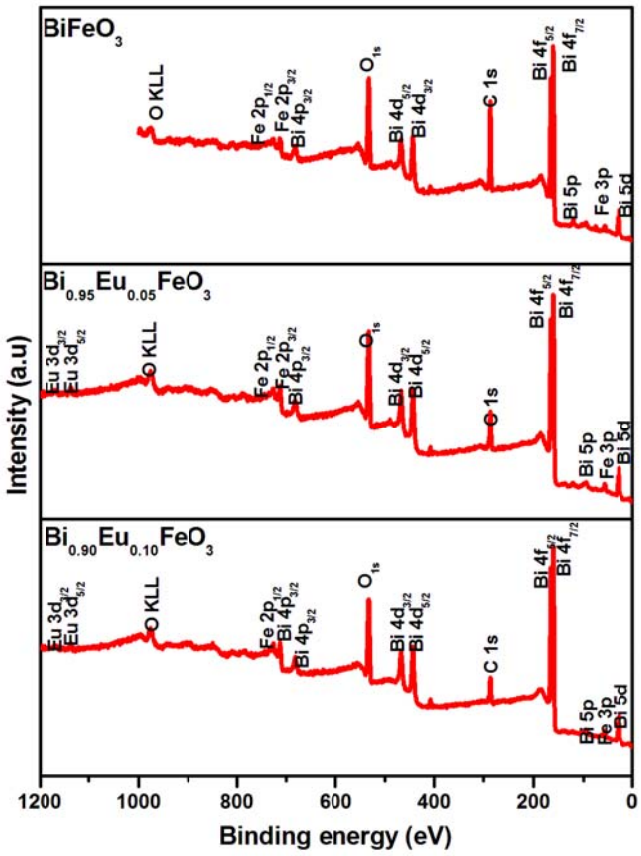

Fig.6 XPS survey spectra of BFO and EBFO samples

Therefore, the investigation of Bi 4f narrow scan spectra is necessary for detailed study, as shown in Fig. 7a. For pure BFO, doublet of Bi 4f signals were de-convoluted into peak of Bi $4f_{5/2}$–O and Bi $4f_{7/2}$–O at 158.5 eV and 163.8 eV, respectively, with spin orbital splitting energy of 5.34 eV, which is in agreement with the reported value.[20] As compared to pure BFO, the corresponding peaks in the 10% Eu-substituted BFO were slightly shifted to 158.6 eV and 163.9 eV with spin orbital splitting energy of 5.31 eV. There is an obvious shift observed toward higher binding energy for Eu-substituted BFO, which could be explained using the phenomenon reported by Wei Liu Zuci Quan et al [11] The shifting Bi 4f peak values due to Ce were interpreted on the basis of electronegativity Bi and O elements. In this case, Eu was substituted at Bi site whose effect can be derived from the eletronegativity of Eu ions and evaluating the covalency/ionicity of Bi–O and Eu–O bonds.

The fraction of covalency can be determine by [21]

$$F_c = \exp[-(\Delta EN)^2/4] \quad \text{---------- Eq. (1)}$$

Where ΔEN is the difference in the anion and cation electro negativities expression for the fraction of ionicity can be given as [21]

$$F_i = 1 - F_c \text{ ---------- Eq. (2)}$$

From the above equations, the obtained F_c and F_i values of Bi–O and Eu–O are listed out in the Table 2.

Table 2 Fraction of covalency F_c and fraction of ionicity F_i for Bi–O, Eu–O, and Fe–O bonds

Parameter	Bi	Eu	Fe	O
Electronegativity	2.02	1.2	1.83	3.44
F_c	0.60	0.28	0.52	
F_i	0.40	0.72	0.48	

Table 2 signifies that the value of F_i for Eu–O (0.72) was much larger than Bi–O (0.40) indicating higher binding energy value for (Bi, Eu)–O than that of Bi–O bond. Therefore, the observed shift in the binding energy of EBFO toward higher order was essentially attributing the substitution of Eu in Bi sites.

To evaluate the oxidation state of Fe, the narrow scan XPS spectrum of Fe 2p line for the pure and Eu-substituted BFO are shown in Fig.7b. From the spectrum, it was observed that Fe 2p orbital into Fe $2p_{3/2}$ and Fe $2p_{½}$ can be observed. These sub peaks could be possibly de-convoluted into two peaks as 711.4eV, 710.0 eV for pure, and 711.9, 710.5 for Eu-substituted BFO. Generally, the oxidation states of Fe^{3+} and Fe $^{2+}$ have reported binding energy values of 711 eV and 709 eV, respectively.[20,22] In our experiment, the Fe ions were found to have a mixture of 3+ and 2+ oxidation states in pure and Eu-substituted BFO. However, the Fe^{2+} ions are unavoidable in BFO owing to the air atmospheric annealing which introduces defects in the form of oxygen vacancies for charge balancing.

From the percentage area under the peak obtained from fitting, the Fe spectrum about 27% and 18% of Fe ions were found be possessed Fe^{2+} oxidation state in pure and Eu substituted BFO respectively. The observed lower concentration of Fe^{2+} ions in EBFO signifies the reduced oxygen defects in the material. A few reports[23, 24] provide an insight into the investigation of oxygen vacancy concentration in perovskite metal oxide materials from O 1s spectra. Consequently, the percentage of oxygen vacancy in pure and Eu-substituted BFO was estimated from the de-convoluting O 1s peak into three peaks as shown in Fig.7c. The lower binding (LB) energy, medium binding (MB) energy and higher binding (HB) energy of pure and Eu-substituted BFO were attributed to the oxygen present in the lattice, oxygen loss and absorbed oxygen on the surface respectively. The percentage of oxygen vacancy concentration can be calculated by taking the ratio MB/LB, from which the values obtained for pure and Eu-substituted BFO were 35% and 28% respectively. Hence, it was evident that the oxygen vacancy concentration was effectively reduced by Eu substitution[25]. The Convoluted peaks of Bi 4f, Fe 2p and O 1s were given in Table 3.

In addition to this, the Iodometric chemical titration analysis was also carried out in order to quantify the oxygen content in pure BFO (2.85) and EBFO (2.91) samples. From the analysis, the oxygen content was found to be rich in EBFO compared to pure BFO. This clearly indicated that the oxygen vacancy was reduced due to the Eu substitution in BFO.

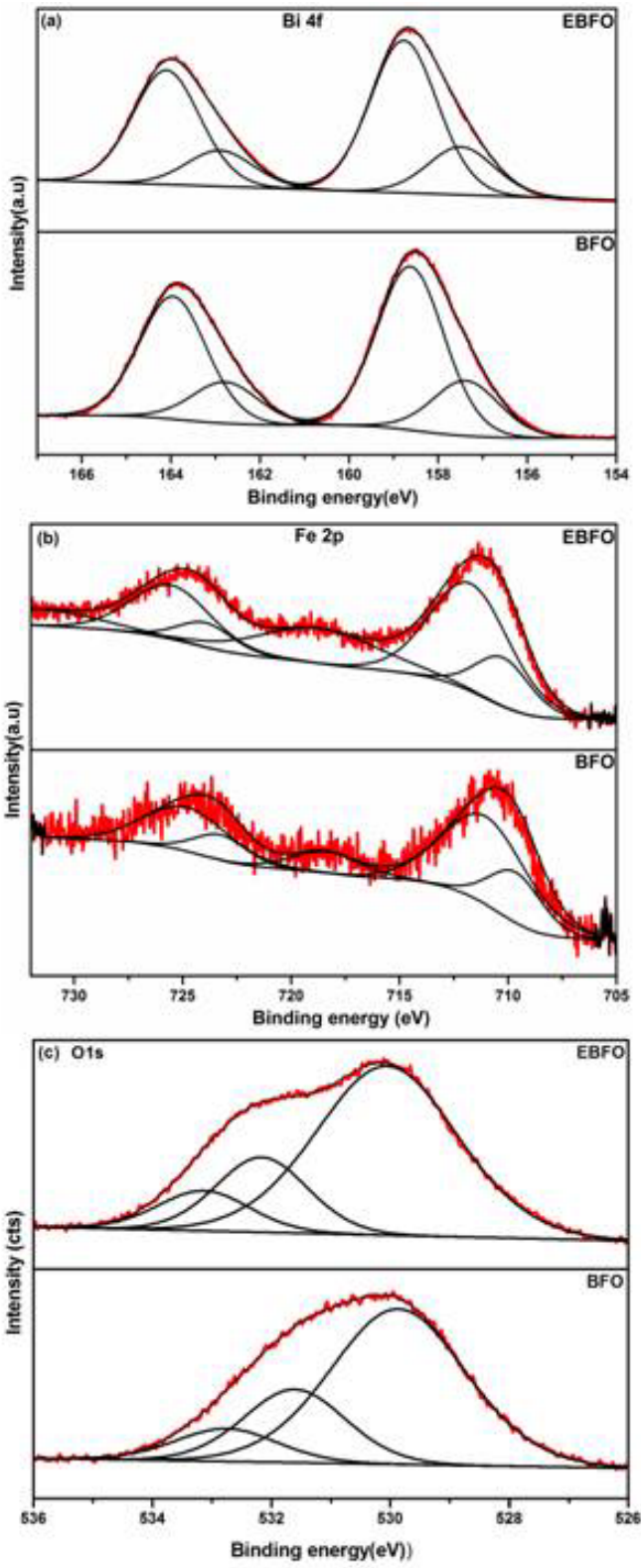

Fig.7 Narrow scan spectra of (a) Bi 4f (b) Fe 2p and (c) O1s.

Table 3 Convoluted peaks of Bi 4f, Fe 2p and O 1s

Samples	Elements	Convoluted		Deconvoluted peaks(eV)	Area	FWHM
		Peaks	Energy position(eV)			
BFO	Bi 4f	5/2	158.4	157.4	8084.2	1.775
				158.6	23990.4	1.775
		7/2	163.8	162.8	6063.1	1.775
				163.9	17992.8	1.775
	Fe 2p	1/2	710.5	710.	1462.7	2.876
				711.4	4075.6	4.599
		3/2	724.2	723.5	731.4	2.876
				725.2	2037.8	4.599
	O1s			529.8	17697.1	2.677
				531.6	6323.5	2.026
				532.7	3047.3	2.026
EBFO	Bi 4f	5/2	158.6	157.5	13421.6	1.778
				158.7	42751.5	1.778
		7/2	163.9	162.9	10066.2	1.778
				164.1	32063.6	1.778
	Fe 2p	1/2	711.4	710.5	2431.9	2.932
				711.9	11126.9	4.303
		3/2	725	724.3	1215.6	2.932
				725.7	5563	4.303
	O1s			530	31278	2.79
				532.2	9046	1.8208
				533.1	4844	1.8208

.

Magnetic properties

In order to investigate the magnetic properties of pure and Eu-substituted BFO samples, the VSM measurements were carried out at room temperature. Fig.8 shows the measurement of magnetization (M) of pure and 10% Eu substituted BFO as a function of applied field (H). Weak magnetic hysteresis behavior was observed for pure BFO with a magnetization value of 70.25 m emu/g at the maximum field of 1 T due to existence of canted antiferromagnetic spins (weak ferromagnetic). As generally reported[4] bulk BFO exhibits antiferromagnetism without any saturation magnetization. Hence, weak ferromagnetism exhibited was due to the pure BFO nanoparticles. With substitution of 10% Eu, an enhancement in magnetization value, 88.04m emu/g, at the maximum field of 1T was observed. A similar behavior has been reported for Eu-substituted $BiFeO_3$[26].

Enhancement of magnetic behavior with Eu substitution can be attributed to structural distortion leading to collapse and suppression of the space modulated cycloid spin structure, as property exhibited by other rare earth ions.[27] With Eu substitution, the structural distortion occurs that results in the canting of spins and therefore bond angle of Fe–O–Fe changes from 159.9° to 158.78°, calculated using BondSTR (FULLPROF). consequently, an increase in the canting angle modifies the magnetic properties, as reported in related literature.[28]

The change in bond angle is an important factor when structural distortion is considered. Up to 10% Eu substitution, there was a suppression of spiral spin structure alone. According to the Landau–ginzburg[29],[30] theory, destruction of spin cycloid in BFO leads to enhanced magneto-electric interaction which can improve the effective magnetic susceptibility and ferroelectric remanent polarization of multiferroics.

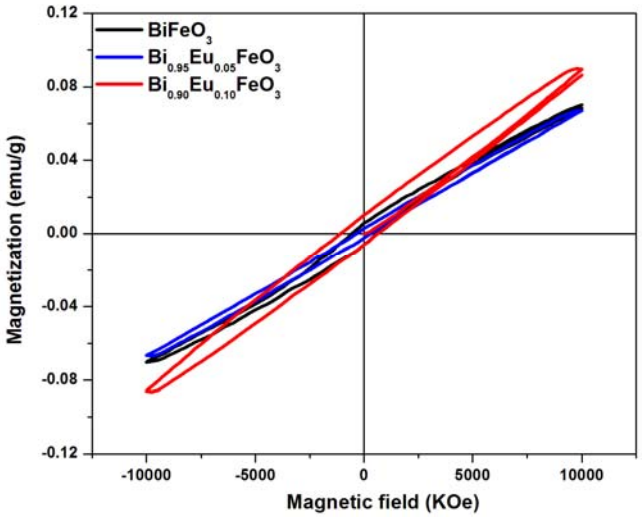

Fig.8 Magnetization(M) vs Magnetic field(H) for BFO and EBFO.

Electric properties

The electric properties of pure and Eu-substituted BFO were analyzed by using impedance spectroscopy. Generally, impedance spectroscopy data can be analyzed using four possible complex interrelated formalisms, that is, Impedance (Z^*), modulus (M^*), permittivity (ε^*), and admittance (A^*)[31]. In general, dielectric material kept in an electric field polarization occurs at a certain frequency. As the field is reversed, dipole reorientation becomes out of phase resulting in energy dissipation and this effect is known as dielectric relaxation. The time delay involved is known as the dielectric relaxation time. This dielectric relaxation occurs at various frequencies for different materials, which is dependent on the type of defect related to the dipoles,

that is, physical or chemical defect.[32] From earlier discussions, it is observed that oxygen vacancy is one of the defects present in BFO. Eventually oxygen vacancy plays an important role in the electrical relaxation of pervoskite materials and it influences the dielectric relaxation behavior at high temperatures due to its increase in oxygen vacancy concentration.[33] There is a decrease in oxygen vacancy concentration with Eu substitution in BFO possibly affecting the dielectric relaxation behavior that was studied using the impedance spectroscopy. The modulus formalism has an added advantage of suppressing the electrode polarization effect. The variation of imaginary part of electric modulus (M*) as a function of frequency over a temperature range of 90°C to 180°C for pure and Eu-substituted are shown in Fig. 9 (a) and (b).

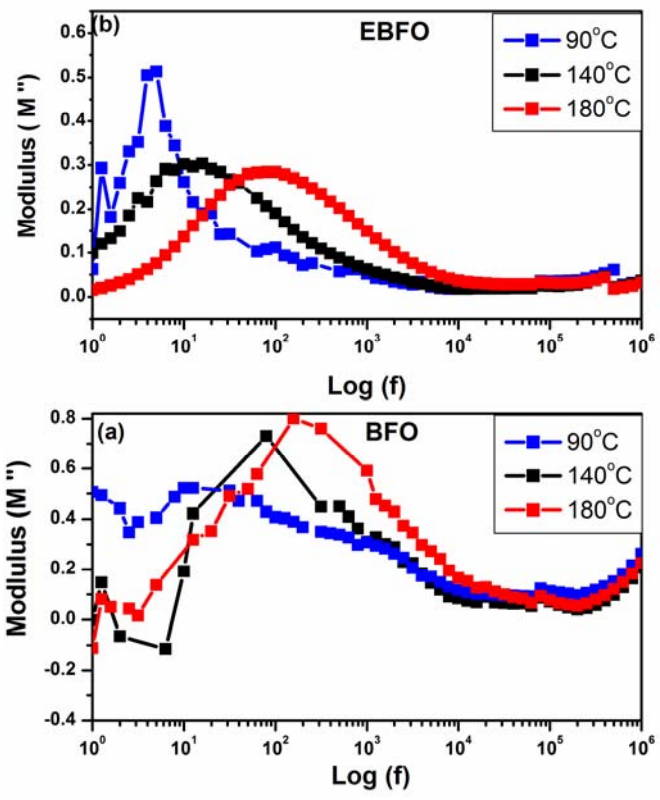

Fig. 9 Modulus spectra of (a) BFO and (b) EBFO

As observed from the spectra, relaxation peaks were shift toward higher frequency with increasing temperature. This was essentially attributing the increase in relaxation rate. The dielectric relaxation time is calculated using the relation,

$\tau_m = 1/(\omega_m)$

where τ_m = relaxation time and ω_m = angular frequency of the materials. This relaxation time as a function of temperature is shown in Fig. 10. As temperature increases, the relaxation time decreases for both the samples attributed to the semiconducting nature of the samples. The activation energy (E_a) was determined from the relaxation time plot using the Arrhenius relation given by,

$\tau_m = \tau_o \exp(-E_a/k_B T)$

Where τ_o is the pre-exponential factor of the relaxation time, T is the temperature, and k_B is the Boltzmann constant

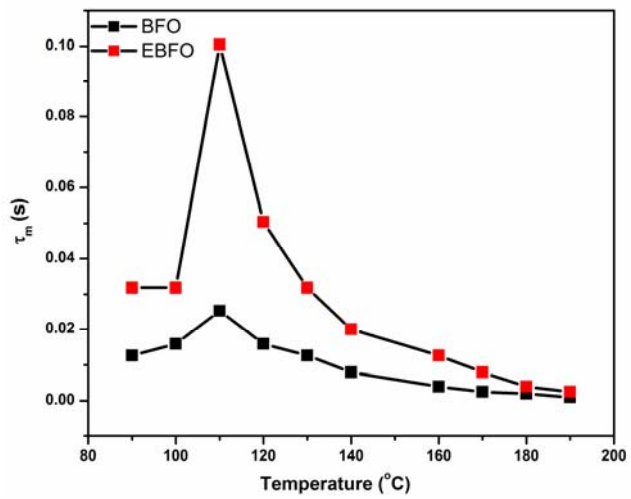

Fig. 10 Dielectric relaxation time vs temperature of BFO and EBFO

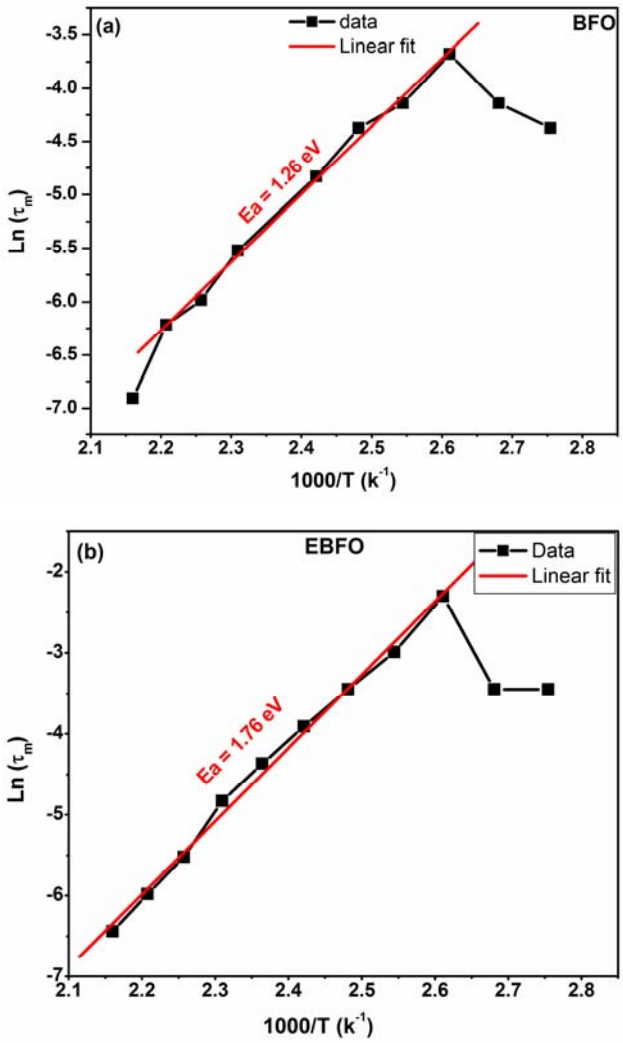

Fig.11 Activation energy of (a) BFO and (b) EBFO

The activation energy (E_a) was determined from the slope of the linear fit in Arrhenius plot, shown in Fig. 11. The values for pure and Eu-substituted BFO are 1.26 eV and 1.76eV, respectively. These values match well with the literature reports.[34] On this basis, the stoichiometric BFO activation energy is 2 eV,[35]

whereas, in this study activation energy was lower due to existence of oxygen vacancy. In Eu-substituted samples, activation energy has increased dramatically. Hence, lead to the suppression of oxygen vacancy.

Conclusions

In summary, this study investigates the dielectric relaxation behavior, activation energy, and magnetic properties of sol-gel derived pure and Eu-substituted BFO nanoparticles. The results were interpreted by estimating the oxygen vacancy and change in the Fe–O–Fe bond angle. XRD studies evidently confirms the rhombohedral space group of R3c and the Rietveld refinement confirms the structural distortion as well as induced changes in lattice parameter and Fe–O–Fe angle with Eu substitution. An increase of canting angle (i.e., decrease of Fe–O–Fe bond angle) with Eu substitution alters the magnetic properties of BFO. The observations of XPS narrow scan of Fe 2p and O1s spectra revealed that the oxygen vacancies were reduced with Eu substitution. Further, these oxygen vacancies induce the changes in dielectric relaxation time and activation energy with related samples.

Acknowledgements

Authors acknowledge the CSIR and UGC, India for funding this project.

Notes and references

[a] *National center for nanoscience and nanotechnology, University of madras, Guindy campus, Chennai 600 025, India. Fax: 044-22352494/22353309; Tel:044-22202749;*
E-mail: balasuga@yahoo.com
[b] *Department of Physics, Indian institute of madras, Chennai 600 076, India.*
[c] *Department of Nuclear physics, University of madras, Guindy campus, Chennai 600 025, India.*

1. Nicola A. Hill, *J. Phys. Chem. B*, 2000, **104**, 6694.
2. H. Schmid, *Ferroelectrics*, 1994, **62**, 317.
3. J. B. Neaton, J. Wang, H. Zheng, V. Nagarajan, S. B. Ogale, B. Liu, V. Vaithyanathan, D. Viehland, D.G. Schlom, U. V. Waghmare, N. A. Spaldin, M. Wuttig, K. M. Rabe and R. Ramesh, *Science*, 2003, **299**, 1719.
4. C. Ederer and N. A. Spaldin, *Phys. Rev. B*, 2005, **71**, 224103.
5. A. Basumallick, B. Bhushan, S K Bandopadhyay, N Y Vasanthacharya and D. Das, *J. Phys. D: Appl. Phys*, 2009, **42**, 065004.
6. A. Dixit, B. Ramachandran, R. Naik, G. Lawes, and M. S. Ramachandra Rao, *Appl. Phys. Lett*, 2012, **100**, 252902.
7. D. A. Kiselev, V. A. Khomchenko, J. M. Vieira, Li Jian, A. L. Kholkin, Y. G. Pogorelov, A. M. L. Lopes, J. P. Araujo and M. Maglione, *J. Appl. Phys*, 2008, **103**, 024105.
8. G. L. Yuan and Siu Wing Or, *J. Appl. Phys*, 2006, **100**, 024109.
9. Jenn-Ming Wu, Yi-Hsien Leec and Chih-Huang Lai, *Appl. Phys. Lett*, 2006, **88**, 042903.
10. Yao Wang and Ce-Wen Nan, *J. Appl. Phys*, 2008, **103**, 024103.
11. Wei Liu Zuci Quan, Hao Hu, Sheng Xu, Bobby Sebo, Guojia Fang, Meiya Li and Xingzhong Zhao, *J. Appl. Phys*, 2008, **104**, 084106.
12. J. S. Jiang, F. Z. Qian, S. Z. Guo, D. M. Jiang and W. G. Zhang, *J.App.phys*, 2009, **106**, 084312.
13. J. Das, S. K. Pradhan, P. P. Rout, S. K. Das, D. K. Mishra, D. R. Sahu, A. K. Pradhan, V. V. Srinivasu, S. Verma, B. B. Nayak, and B.K.Roul, *J. Magn. Magn. Mater*, 2010, **322**, 3614.
14. Meiya Li Zhongqiang Hu, Jun Liu, Ling Pei, Jing Wang, Benfang Yu, and Xingzhong Zhao, *J. Am. Ceram. Soc*, 2010, **93**, 2743.
15. R. D. Shannon, *Acta Crystallogr*, 1976, **A32**, 751
16. Yan'ge Zhang Xiong Wang and Zhibin Wu, *Mater. Lett.*, 2010, **64**, 486.
17. Xuelian Yu and Xiaoqiang An, *Solid State Commun.*, 2009, **149**, 711.
18. M. B. Bellakki V. Manivannan, *J Sol-Gel Sci Technol*, 2010, **53**, 184.
19. Yu Suia Xingquan Zhang, Xianjie Wanga, Yang Wangc and Zhu Wanga, *J. Alloys Compd*, 2010, **507**, 157.
20. W. F. Stickle J. F. Moulder, P. E. Sobol, and K. D. Bomben, *Perkin-Elmer, Minnesota*, 1992.
21. D. R. Askeland, *PWS, Boston*, 1994.
22. B. A. Kobe, A. P. Grosvenor, M. C. Biesinger and N. S. McIntyre, *Surf. Interface Anal*, 2004, **36**, 1564.
23. Dorota A. Pawlak, Krzysztof Woz´niak, Zygmunt Frukacz, Tery L. Barr, Dean Fiorentino and Steven Hardcastle, *J. Phys. Chem. B*, 1999, **103**, 3332.
24. Hanqing Zhao, Jiaou Wang, Linxing Zhang, Yangchun Rong, Jun Chen, Kurash Ibrahim and Xianran Xing, *Dalton Trans*, 2013, **42**, 10358.
25. Xiaojian Zhu, Fei Zhuge, Mi Li, Kuibo Yin, Yiwei Liu, Zhenghu Zuo, Bin Chen and Run-Wei Li, *J. Phys. D: Appl. Phys*, 2011, **44**, 415104.
26. Jian Liu, Liang Fang, Fengang Zheng, Sheng Ju and Mingrong Shenc, *Appl. Phys.Lett*, 2009, **95**, 022511.
27. Liang Fang, Renqing Guo, Wen Dong, Fengang Zheng and Mingrong Shen, *J. Phys. Chem. C*, 2010, **114**, 21390.
28. A. Scholl 28J. Wang, H. Zheng, S. B. Ogale, D. Viehland, D. G. Schlom, N., K. M. Rabe A. Spaldin, M. Wuttig, L. Mohaddes, J. Neaton, U. and T. Zhao Waghmare, and R. Ramesh,, *Science*, 2005, **307**, 1203b.
29. Benjamin Ruette, S. Zvyagin, A. P. Pyatakov, A. Bush, J. F. Li, V. I. Belotelov, A. K. Zvezdin and D. Viehland, *Phys. Rev. B*, 2004, **69**, 064114.
30. Naigang Wang, J. Cheng, A. Pyatakov, A. K. Zvezdin, J. F. Li, L. E. Cross, and D. Viehland, *Phys. Rev. B*, 2005, **72**, 104434.
31. New York J. R. Macdonald (Wiley, 1987), *Impedance Spectroscopy*.
32. C. Elissalde and J. Ravez, *J. Mater. Chem*, 2001, **11**, 1957.
33. Y. Zhi, A. Chen and L. E. Cross, *Phys. Rev. B*, 2000, **62**, 228.
34. Xiaojie Lou, Qingqing Ke, Yang Wang and John Wang, *Phys. Rev. B*, 2010, **82**, 024102.
35. R. Bugge, S. Steinsvik, J. Gjonnes, J. Tafto and T. Norby, *J. Phys. Chem.Solids*, 1997, **58**, 969.